

Gravity Field of the Orientale Basin from the Gravity Recovery and Interior Laboratory (GRAIL) Mission

Maria T. Zuber^{1*}, David E. Smith¹, Gregory A. Neumann², Sander Goossens³,
Jeffrey C. Andrews-Hanna^{4,5}, James W. Head⁶,
Walter S. Kiefer⁷, Sami W. Asmar⁸, Alexander S. Konopliv⁸,
Frank G. Lemoine², Isamu Matsuyama⁹, H. Jay Melosh¹⁰,
Patrick J. McGovern⁷, Francis Nimmo¹¹, Roger J. Phillips⁵,
Sean C. Solomon^{12,13}, G. Jeffrey Taylor¹⁴, Michael M. Watkins^{8,15},
Mark A. Wieczorek¹⁶, James G. Williams⁸, Johanna C. Jansen⁴,
Brandon C. Johnson^{1,6}, James T. Keane⁹, Erwan Mazarico²,
Katarina Miljkovi^{1,17}, Ryan S. Park⁸, Jason M. Soderblom¹, Dah-Ning Yuan⁸

Submitted to: *Science*
May 5, 2016

Tracking by the GRAIL spacecraft has yielded a model of the gravitational field of the Orientale basin at 3–5-km horizontal resolution. The diameter of the basin excavation cavity closely matches that of the Inner Depression. A volume of at least $(3.4 \pm 0.2) \times 10^6 \text{ km}^3$ of crustal material was removed and redistributed during basin formation; the outer edges of the zone of uplifted mantle slope downward and outward by 20° – 25° . There is no preserved evidence of the transient crater that would reveal the basin's maximum volume,

¹Department of Earth, Atmospheric and Planetary Sciences, Massachusetts Institute of Technology, Cambridge, MA 02139-4307, USA.

²Solar System Exploration Division, NASA Goddard Space Flight Center, Greenbelt, MD 20771, USA.

³Center for Research and Exploration in Space Science and Technology, University of Maryland, Baltimore County, Baltimore, MD 21250, USA.

⁴Department of Geophysics and Center for Space Resources, Colorado School of Mines, Golden, CO 80401, USA.

⁵Southwest Research Institute, Boulder, CO 80302, USA.

⁶Department of Earth, Environmental and Planetary Sciences, Brown University, Providence, RI 02912, USA

⁷Lunar and Planetary Institute, Houston, Texas 77058, USA.

⁸Jet Propulsion Laboratory, Pasadena, CA 91109, USA.

⁹Lunar and Planetary Laboratory, University of Arizona, Tucson, AZ 85721-0092, USA

¹⁰Department of Earth, Atmospheric and Planetary Sciences, Purdue University, West Lafayette, IN 47907, USA.

¹¹Department of Earth and Planetary Sciences, University of California, Santa Cruz, Santa Cruz, California 95064, USA.

¹²Department of Terrestrial Magnetism, Carnegie Institution of Washington, Washington, DC 20015, USA.

¹³Lamont-Doherty Earth Observatory, Columbia University, Palisades, NY 10964, USA.

¹⁴Hawaii Institute of Geophysics and Planetology, University of Hawaii, Honolulu, HI 96822, USA.

¹⁵Center for Space Research, University of Texas, Austin, TX 78712 USA.

¹⁶Institut de Physique du Globe de Paris, Sorbonne Paris Cité, Université Paris Diderot, 75205 Paris Cedex 13, France.

¹⁷Department of Applied Geology, Curtin University, Perth, WA 6845, Australia.

*To whom correspondence should be addressed: zuber@mit.edu

but its diameter may now be calculated from the observed structure to be between the diameters of the Inner Depression and Inner Rook ring. The model resolves distinctive structures of Orientale's three rings, including their azimuthal variations, and suggests the presence of faults that penetrate the crust. The crustal structure of Orientale provides constraints in the third dimension on models for the formation of multi-ring basins.

Basin-scale impacts disrupted early planetary crusts and imparted substantial kinetic energy that was manifest in fracturing, melting, vaporization, seismic shaking, ejection, and re-distribution of crustal and possibly mantle material. Impact basins preserve the record of these planet-altering events, and the study of these structures elucidates the partitioning of energy and its corresponding geological and environmental effects early in planetary history. Surface signatures of impact basins on solid planets have been extensively documented (1, 2), but their subsurface structure has, to date, been poorly characterized. Here we present the highest-resolution orbital gravity field model of any major impact basin – the Orientale basin on the Moon – as mapped by the Gravity Recovery and Interior Laboratory (GRAIL) mission (3).

Orientale, located on the western limb of the lunar nearside, is the youngest (~ 3.8-Gy old) (1, 4) large (~930-km-diameter) impact basin on the Moon. As a consequence of its good state of preservation (1, 5), with relatively few superposed large craters (6), it is often considered the standard example of a well-preserved, multi-ring basin in comparative studies of large impacts on terrestrial planetary bodies (2, 7). Because of the basin's importance, the GRAIL Extended Mission (XM; see SOM) featured a low-altitude mapping campaign during the mission's Endgame phase (8), in which the dual spacecraft orbited the Moon at an average altitude of 6 km and acquired observations less than 2 km above the basin's eastern rings (Figs. S1 and S2).

To realize the highest-resolution gravity map achievable from the data and to assure that small-scale features resolved were robust, we developed two maps that used the same data but independent methodologies (see SOM). The first is a global spherical harmonic expansion of GRAIL's Ka-band range-rate (KBRR) tracking data to degree and order 1200 (spatial block size = 4.5 km). The second is a local model that implemented a short-arc analysis (9) of the tracking data and used a gravitational field model to degree and order 900 (10) as the *a priori* field. Local gravitational anomalies were estimated with respect to the spherical harmonic model at the center coordinates of the grid points. The final model has a mixed grid resolution $0.1^\circ \times 0.1^\circ$ and $0.1667^\circ \times 0.1667^\circ$, with maximum spatial resolution varying between 3 and 5 km. These independent analyses produced gravitational models of Orientale that are essentially indistinguishable (cf. Fig. S4). The maps in Fig. 1 resolve the shallow subsurface structure of Orientale at a spatial resolution comparable with that of many geological structures at the surface, including simple and secondary craters.

The topography of the Orientale basin from the Lunar Orbiter Laser Altimeter (11) and the free-air gravity anomaly field of the region are shown in Figs. 1A and 1B. The maps show similar detail at small spatial scales because above degree and order 80 (spatial block size < 68 km) >98% of the lunar gravity field is attributable to topography (12). The high correlation of topography and gravity at short horizontal scales is due to the large magnitude of the gravity anomalies arising from topography relative to the

weaker anomalies arising from density anomalies in the shallow subsurface (12). Removal of the gravitational signature associated with topography clearly resolves structure within the lunar crust.

Both topography and free-air gravity anomaly resolve Orientale's Inner Depression (ID), as well as the Inner Rook ring (IRR), Outer Rook ring (ORR), and Cordillera ring (CR). The rings, partially resolved in pre-GRAIL gravitational models with an order of magnitude poorer spatial resolution and multiple orders of magnitude lower signal sensitivity than those in this study (13), formed in the process of cavity collapse during the modification stage of the impact event, within an hour of the initiation of basin formation (14). The mechanism for ring formation, however, has been controversial (2, 5, 15-17), in large part because of a lack of understanding of subsurface structure needed to provide constraints on impact basin formation models.

At larger spatial scales, a greater fraction of the gravitational signal is associated with mass variations within the Moon. These variations are best revealed in the Bouguer gravity anomaly field (Fig. 1C), a representation of the gravitational field after the attraction of surface topography has been removed.

For uniform-density crust and mantle (2550 and 3220 kg m^{-3} , respectively), the Bouguer gravity anomaly can be downward continued and used to map the crust-mantle boundary, to yield crustal thickness (Fig. 1D, Fig. S5). Although the assumption of uniform density is an approximation, its application to the regional crustal structure is supported by crustal density inferred from GRAIL (18) as well as from orbital remote sensing data (see SOM and Fig. S6). Some models for the crust invoke a mixed feldspathic layer that overlies a layer of pure anorthosite (19), but the density contrast between these rock types is small in comparison with that across the crust-mantle interface.

A cross-section of crustal structure along the profile in Fig. 1D is shown in Fig. 2. Crust-mantle boundary profiles take into account the effect on the crustal structure of a 10-km-thick sheet of density 2650 kg m^{-3} appropriate for crustal impact melt or crustal material formed by differentiation of Orientale's melt pool (see SOM); in the end-member case in which the sheet is instead identical in density to feldspathic crust, the minimum crustal thickness would be only 2 km less. Consequently, the presence of a high-density sheet does not have a substantial effect on the basin's crustal structure. Fig. 1D indicates that the Orientale impact removed and redistributed a minimum of $(3.4 \pm 0.2) \times 10^6 \text{ km}^3$ of material (see SOM) from the lunar crust. Approximately one-third of the excavated material was deposited as ejecta in an annulus between the Cordillera ring and a radial distance from the basin center of one basin diameter (20), contributing to enhanced crustal thickness in this region (Fig. 1D). The high porosity ($\sim 18\%$) observed in the Orientale ejecta blanket (18, 21) is similar to the porosity observed in Apollo 14 samples of the Fra Mauro Formation, which consist of ejecta from the Imbrium basin (22).

The calculation of crustal thickness does not include the presence of the mare units that are generally less than 1 km thick and irregularly distributed within the Inner Depression and ponded irregularly inside the Outer Rook and Cordillera rings (21) (low-reflectance areas in Fig. S7). The gravitational signal of the mare units is partially masked by the unknown characteristics of the impact melt sheet, and where these deposits are present, the underlying crustal thickness would be slightly greater than in the model.

Pre-GRAIL gravitational models have shown that the most distinct, well-preserved, large-scale gravitational signature associated with large lunar basins is a strong central positive free-air anomaly (23-26). These mass excesses or mascons (27) are a consequence of the thinning of the crust beneath the basin combined with the super-isostatic uplift of a central basin that was mechanically coupled to initially sub-isostatic surrounding material (28, 29). Figs. 1 and 2 show that in Orientale, the diameter of crustal thinning corresponds closely to the diameter of the Inner Depression. We therefore identify the Inner depression as an approximation to the basin excavation cavity.

Of great interest in impact studies is the transient crater – the cavity formed at the culmination of excavation, prior to collapse and modification. The transient crater represents the time corresponding to the maximum displaced volume, and its diameter satisfies standard impact scaling laws (30, 31), which allow many characteristics of an impact to be inferred from its size. From previous analyses ranging from geological mapping to numerical simulation, each of Orientale’s basin rings have been variously interpreted as marking the diameter of the transient crater (2, 5, 15, 16, 32). GRAIL’s greatly improved spatial resolution and signal sensitivity compared with all previous models of the internal structure of Orientale, in contrast, show no evidence of the transient crater, indicating that any remnant is not preserved or at least not recognizable in the gravity field. However, the transient crater diameter may now be calculated with confidence from scaling laws (33). From the 530-km diameter of crustal thinning (Fig. 1D) measured from an azimuthally averaged crustal thickness profile (Fig. S5), the transient crater diameter is between 320 and 460 km, placing it between the diameters of Orientale’s Inner Depression and Inner Rook ring. The transient crater thus does not correlate with a specific ring; indeed, hydrocode modeling constrained by this crustal structure model (14) indicates that rings form subsequent to the transient crater, during the collapse phase.

The sharp transition between the basin excavation cavity and the surrounding crust is well illustrated in Fig. 2. At the outer edges of the zone of mantle uplift, the crust-mantle boundary slopes outward and downward by 20°–25°. The spatial correspondence of this plug of uplifted mantle with the Inner Depression is similar to the pattern seen in other multi-ring basins (34), but is in contrast to peak-ring basins, where the zone of uplifted mantle is limited to within the peak ring (35).

The model also shows, beyond the basin depression, an annulus of thickened crust (Figs. 1D and S8D) and radial structure in gravity gradients (Figs. 1E and S8E) that correlate with observed ejecta structures (e.g., secondary crater chains) (20).

Aspects of Orientale’s asymmetry in surface structure extend to the subsurface, as indicated in Figs. 1 and 2. For instance, the basin exhibits an east–west variation in regional crustal structure that predated formation of the basin. There are also azimuthal variations in crustal thickness, some of which are distinctly associated with basin rings. The simplest interpretation of the azimuthally averaged models is that they could correspond to displacements associated with normal faults that penetrate the crust. The crust-mantle boundary relief in Fig. 2B suggests there could be multiple faults dipping inward from the Outer Rook and Cordillera rings. The crustal thickness model also suggests the presence of other crustal faults that lack a visible surface expression. Although these faults may be listric, i.e., the dip angle decreases with depth, a dip of 50°,

indicated by hydrocode simulations (14), is consistent with prominent changes in crust–mantle boundary depth. The simulations also support crustal faulting not associated with rings.

Insight into the distinctive nature of each ring can be gained from scrutiny of Figs. 1, 2, and S8. The Inner Depression has the most axisymmetric and the largest variation in crustal thickness as well as a change in the sign of the gravity gradient. The Inner Rook ring has a well-developed topographic expression. Individual peaks within the Inner Rook are associated with positive free-air and Bouguer anomalies embedded within an annulus of negative free-air and Bouguer anomalies. The Inner Rook also appears associated with a near-circumferentially continuous change in the sign of the gravity gradient (Fig. 1E) and a flattening in relief along the crust–mantle boundary.

The Outer Rook ring also displays well-developed topography and associated positive free-air anomalies embedded within the same annulus of negative free-air and Bouguer anomalies. The most negative Bouguer gravity in the region appears within the Outer Rook and may reflect a combination of thickening of the crust by ejecta and extensive fracturing in the crustal column. The Outer Rook displays a sign change in the gravity gradient and a mild shoaling of the crust–mantle boundary. These characteristics of the Outer Rook ring are also consistent with local thinning of the crust associated with faulting.

The topography of the Cordillera ring deviates markedly from axisymmetry; it is less developed than the Inner and Outer Rook rings and has little expression in part of the basin's southwestern quadrant. This asymmetric structure may be a consequence of the northeast-to-southwest-directed oblique impact that formed the basin (36) or pre-existing heterogeneity of crustal or lithospheric structure (2, 37), with a clear west-to-east gradient of decreasing crustal thickness still preserved (Fig. 1D). The ring is characterized by positive free-air and Bouguer anomalies, a gradient in crustal thickness, and a circumferentially discontinuous sign change in the gravity gradient. The variation of relief along the crust–mantle boundary strongly suggests fault penetration to the lower crust and possibly upper mantle. The gravitational signature could alternatively reflect contributions from magmatic intrusions along the irregularly developed ring fault, but regional seismic reflection profiles of a portion of the terrestrial Chicxulub impact structure, 20%-25% the size of Orientale, show ring faults that extend well into the lower crust (38).

A hydrocode calculation (14) constrained by the high-resolution observations reported here successfully reproduces the major characteristics of Orientale's crustal structure and elucidates the thermal, tectonic, and geological consequences of the largest impacts that dominated the earliest evolution of the Moon and other solid planets.

References and Notes

1. D. E. Wilhelms, *The Geologic History of the Moon*. U.S. Geol. Survey Prof. Paper 1348 (US Govt. Printing Office, Washington, DC, 1987), 302 pp.
2. P. D. Spudis, *The Geology of Multiring Impact Basins: The Moon and Other Planets*. (Cambridge Univ. Press, Cambridge, England, 1993), 277 pp.
3. M. T. Zuber, D. H. Lehman, D. E. Smith, T. L. Hoffman, S. W. Asmar, Gravity Recovery and Interior Laboratory (GRAIL): Mapping the lunar interior from crust to core. *Space Sci. Rev.* **178**, doi: 10.1007/s11214-012-9952-7 (2013).

4. D. Stoffler *et al.*, Cratering history and lunar chronology. *Rev. Mineral. Geochem.* **60**, 519 (2006).
5. J. W. Head, Orientale multi-ringed basin interior and implications for the petrogenesis of lunar highland samples. *Moon* **11**, 327 (1974).
6. C. I. Fassett *et al.*, Lunar impact basins: Stratigraphy, sequence and ages from superposed impact crater populations measured from Lunar Orbiter Laser Altimeter (LOLA) data. *J. Geophys. Res.* **117**, doi: 10.1029/2011JE003951 (2012).
7. K. A. Howard, D. E. Wilhelms, D. H. Scott, Lunar basin formation and highland stratigraphy. *Rev. Geophys. Space Phys.* **12**, 309 (1974).
8. T. H. Sweetser, M. S. Wallace, S. J. Hatch, R. B. Roncoli, in *AIAA Astrodynamics Specialist Conference*. (Minneapolis, MN, 2012), 18 pp.
9. D. D. Rowlands, R. D. Ray, D. S. Chinn, F. G. Lemoine, Short-arc analysis of intersatellite tracking data in a gravity mapping mission. *J. Geod.* **76**, 307 (2002).
10. F. G. Lemoine *et al.*, A degree-900 lunar gravity model from GRAIL primary and extended mission data. *Geophys. Res. Lett.* **41**, 3382 (2014).
11. D. E. Smith *et al.*, The Lunar Orbiter Laser Altimeter investigation on the Lunar Reconnaissance Orbiter mission. *Space Sci. Rev.* **150**, 209 (2010).
12. M. T. Zuber *et al.*, Gravity field of the Moon from the Gravity Recovery and Interior Laboratory (GRAIL) mission. *Science* **339**, doi: 10.1126/science.1231507 (2013).
13. Y. N. Kattoum, J. C. Andrews-Hanna, Evidence for ring-faults around the Orientale basin on the Moon from gravity. *Icarus* **226**, 694 (2013).
14. B. C. Johnson *et al.*, The formation of the Orientale lunar multi-ring basin. *Science*, (2016).
15. J. W. Head, in *Impact and Explosion Cratering*, D. J. Roddy, R. O. Pepin, R. B. Merrill, Eds. (Pergamon Press, New York, NY, 1977), pp. 563-573.
16. C. A. Hodges, D. E. Wilhelms, Formation of lunar basin rings. *Icarus* **34**, 294 (1978).
17. J. W. Head, Transition from complex craters to multi-ringed basins on terrestrial planetary bodies: Scale-dependent role of the expanding melt cavity and progressive interaction with the displaced zone. *Geophys. Res. Lett.* **37**, doi: 1029/2009GL041790 (2010).
18. M. A. Wieczorek *et al.*, The crust of the Moon as seen by GRAIL. *Science* **339**, doi: 10.1126/science.1231530 (2013).
19. M. A. Wieczorek, R. J. Phillips, Lunar multiring basins and the cratering process. *Icarus* **139**, 246 (1999).
20. C. I. Fassett, J. W. I. Head, D. E. Smith, M. T. Zuber, G. A. Neumann, Thickness of proximal ejecta from the Orientale Basin from Lunar Orbiter Laser Altimeter (LOLA) data: Implications for multi-ring basin formation. *Geophys. Res. Lett.* **38**, doi:10.1029/2011GL048502 (2011).
21. J. Besserer *et al.*, GRAIL gravity constraints on the vertical density structure of the lunar crust. *Geophys. Res. Lett.* **41**, doi: 10.1002/2014GL060240 (2014).
22. W. S. Kiefer, R. J. Macke, D. T. Britt, A. J. Irving, G. J. Consolmagno, The density and porosity of lunar rocks. *Geophys. Res. Lett.* **39**, doi:10.1029/2012GL051319 (2012).
23. M. T. Zuber, D. E. Smith, F. G. Lemoine, G. A. Neumann, The shape and internal structure of the Moon from the Clementine mission. *Science* **266**, 1839 (1994).
24. G. A. Neumann, M. T. Zuber, D. E. Smith, F. G. Lemoine, The lunar crust: Global signature and structure of major basins. *J. Geophys. Res.* **101**, 16,841 (1996).
25. A. S. Konopliv *et al.*, Gravity field of the Moon from Lunar Prospector. *Science* **281**, 1476 (1998).
26. N. Namiki *et al.*, Farside gravity field of the Moon from four-way Doppler measurements of SELENE (Kaguya). *Science* **323**, 900 (2009).
27. P. M. Muller, W. L. Sjogren, Mascons: Lunar mass concentrations. *Science* **161**, 680 (1968).
28. J. C. Andrews-Hanna, The origin of the non-mare mascon gravity anomalies in lunar basins. *Icarus* **222**, 159 (2013).
29. H. J. Melosh *et al.*, The origin of lunar mascon basins. *Science* **340**, 1552 (2013).
30. R. M. Schmidt, K. R. Housen, Some recent advances in the scaling of impact and explosion cratering. *Int. Jour. Impact Eng.* **3**, 543 (1987).

31. B. A. Ivanov, H. J. Melosh, E. Pierazzo, in *Large Meteorite Impacts and Planetary Evolution*, R. L. Gibson, W. U. Reimold, Eds. (Geol. Soc. Am., Boulder, CO, 2010), pp. 29-49.
32. R. W. K. Potter, D. A. Kring, G. S. Collins, W. S. Kiefer, P. J. McGovern, Numerical modeling of the formation and structure of the Orientale impact basin. *J. Geophys. Res.* **118**, 1 (2013).
33. R. W. K. Potter, D. Kring, G. S. Collins, W. S. Kiefer, P. J. McGovern, Estimating transient crater size using the crustal annular bulge: Insights from numerical modeling of lunar basin-scale impacts. *Geophys. Res. Lett.* **39**, doi:10.1029/2012GL052981 (2012).
34. G. A. Neumann *et al.*, Lunar impact basins revealed by the Gravity Recovery and Interior Laboratory measurements. *Sci. Advances* **1**, doi: 10.1126/sciadv.1500852 (2015).
35. D. M. H. Baker *et al.*, GRAIL gravity analysis of peak-ring basins on the Moon: Implications for the crater to basin transition. *Lunar Planet. Sci. Conf.*, #2662 (2013).
36. J. F. McCauley, Orientale and Caloris. *Phys. Earth Planet. Int.* **15**, 220-250 (1977).
37. A. Nahm, T. Öhman, D. Kring, Normal faulting origin for the Cordillera and Outer Rook Rings of Orientale Basin, the Moon. *J. Geophys. Res.* **118**, 190 (2013).
38. S. P. S. Gulick *et al.*, Geophysical characterization of the Chicxulub impact crater. *Rev. Geophys. Space Phys.* **51**, 31 (2013).
39. S. J. Hatch, R. B. Roncoli, T. H. Sweetser, in *AIAA Astrodynamics Conf.* (Toronto, CA, 2010), vol. AIAA 2010-8385, 8 pp.
40. J. G. Beerer, G. G. Havens, paper presented at the SpaceOps 2012, 11-15 June 2012.
41. A. S. Konopliv *et al.*, The JPL lunar gravity field to degree 660 from the GRAIL primary mission. *J. Geophys. Res.* **118**, doi:10.1002/jgre.20097 (2013).
42. F. G. Lemoine *et al.*, High-degree gravity models from GRAIL primary mission data. *J. Geophys. Res.* **118**, doi: 10.1002/jgre.20118 (2013).
43. A. S. Konopliv *et al.*, JPL high resolution lunar gravity fields from the GRAIL Primary and Extended mission. *Geophys. Res. Lett.* **41**, 1452 (2014).
44. R. S. Park *et al.*, paper presented at the *Am. Geophys. Un. Fall Meeting*, San Francisco, CA, (2014).
45. D. D. Rowlands *et al.*, Resolving mass flux at high spatial and temporal resolution using GRACE intersatellite measurements. *Geophys. Res. Lett.* **32**, doi: 10.1029/2004GL021908 (2005).
46. S. B. Luthcke *et al.*, Monthly spherical harmonic gravity field solutions determined from GRACE inter-satellite range-rate data alone. *Geophys. Res. Lett.* **33**, doi: 10.1029/2005GL024846 (2006).
47. B. D. Tapley, S. Bettadpur, J. C. Ries, P. F. Thompson, M. M. Watkins, GRACE measurements of mass variability in the Earth system. *Science* **305**, doi: 10.1126/science.1099192 (2004).
48. S. Goossens *et al.*, High-resolution local gravity model of the south pole of the Moon from GRAIL extended mission data. *Geophys. Res. Lett.* **41**, 3367 (2014).
49. W. A. Heiskanen, H. Moritz, *Physical Geodesy*. (W.H. Freeman, San Francisco/London, 1967), 403 pp.
50. D. E. Pavlis, J. Wimert, J. J. McCarthy, "GEODYN II System Description," (SGT, 2013).
51. D. D. Rowlands *et al.*, Global mass flux solutions from GRACE: A comparison of parameter estimation strategies -- Mass concentrations versus Stokes coefficients. *J. Geophys. Res.* **115**, doi: 10.1029/2009JB006546 (2010).
52. T. J. Sabaka, D. D. Rowlands, S. B. Luthcke, J.-B. Boy, Improving global mass flux solutions from Gravity Recovery and Climate Experiment (GRACE) through forward modeling and continuous time correlation. *J. Geophys. Res.* **115**, doi: 10.1029/2010JB007533 (2010).
53. A. M. Freed *et al.*, The formation of lunar mascon basins from impact to contemporary form. *J. Geophys. Res.* **119**, 2378 (2014).
54. W. S. Kiefer, R. J. Macke, D. T. Britt, A. J. Irving, G. J. Consolmagno, The density and porosity of lunar impact breccias and impact melt rocks and implications for GRAIL gravity modeling of the Orientale impact basin structure. *Lunar Planet. Sci. Conf.* **XLVI**, (2015).

55. P. D. Spudis, D. J. P. Martin, G. Y. Kramer, Geology and composition of the Orientale Basin impact melt sheet. *J. Geophys. Res.* **119**, 1 (2014).
56. Q. Huang, M. A. Wieczorek, Density and porosity of the lunar crust from gravity and topography. *J. Geophys. Res.* **117**, doi:10.1029/2012JE004062 (2012).
57. D. M. Blair, B. C. Johnson, A. M. Freed, H. J. Melosh, Modeling the geophysical history of very large impact basins: The gravity anomalies of the Orientale basin. *Lunar Planet. Sci. Conf. XLV*, #2105 (2014).
58. Y. Bottinga, D. F. Weill, The viscosity of magmatic silicic liquids: A model for calculation. *American Journal of Science* **272**, 438 (1972).
59. W. S. Kiefer *et al.*, The contribution of impact melt sheets to lunar impact basin gravity anomalies. *Lunar Planet. Sci. Conf. XLV*, # 2831 (2014).
60. W. M. Vaughan, J. W. Head, L. Wilson, P. C. Hess, Geology and petrology of enormous volumes of impact melt on the Moon: A case study of the Orientale basin impact melt sea. *Icarus* **223**, 749 (2013).
61. J. Whitten *et al.*, Lunar mare deposits associated with the Orientale impact basin: New insights into mineralogy, history, mode of emplacement, and relation to Orientale Basin evolution from Moon Mineralogy Mapper (M3) data from Chandrayaan"1. *J. Geophys. Res.* **116**, doi:10.1029/2010JE003736 (2011).
62. G. Ryder, J. A. Wood, Serenitatis and Imbrium impact melts: Implications for large-scale layering in the lunar crust. *Proc. Lunar Planet. Sci. Conf. 8th*, 655 (1977).
63. B. L. Jolliff, J. J. Gillis, L. Haskin, R. L. Korotev, M. A. Wieczorek, Major lunar crustal terranes: Surface expressions and crust-mantle origins. *J. Geophys. Res.* **105**, 4197 (2000).
64. R. L. Korotev, The great lunar hot spot and the composition and origin of the Apollo mafic ("LKFM") impact-melt breccias. *J. Geophys. Res.* **105**, 4317 (2000).
65. J. J. Papike, G. Ryder, C. K. Shearer, in *Planetary materials*, J. J. Papike, Ed. (1998), vol. Rev. Mineral., 36, pp. 5-1 to 5-235.
66. P. G. Lucey, D. T. Blewett, B. J. Jolliff, Lunar iron and titanium algorithms based on final processing of Clementine UVVIS data. *J. Geophys. Res.* **105**, 20,297-20,308 (2000).
67. T. H. Prettyman *et al.*, Elemental composition of the lunar surface: Analysis of gamma ray spectroscopy data from Lunar Prospector. *J. Geophys. Res.* **111**, doi:10.1029/2005JR002656 (2006).
68. S. T. Crites, P. D. Lucey, Revised mineral maps of the Moon from integrating results from the Lunar Prospector neutron and gamma ray spectrometers with Clementine spectroscopy. *Am. Mineral.* **100**, doi:10.2138/am-2015-4874 (2014).
69. P. D. Lucey, Mineral maps of the Moon. *Geophys. Res. Lett.* **31**, doi:10.1029/2003GL019406 (2004).
70. H. J. Moore, C. A. Hodges, D. H. Scott, Multi-ringed basins -- Illustrated by Orientale and associated features. *Proc. Lunar Planet. Sci. Conf. 5th, Geochim. Cosmochim. Acta supp. 5*, 71-100 (1974).
71. S. Yamamoto *et al.*, Massive layer of pure anorthosite on the Moon. *Geophys. Res. Lett.* **39**, doi:10.1029/2012GL052098 (2012).
72. L. C. Cheek, K. L. Donaldson Hanna, C. M. Pieters, J. W. Head, J. L. Whitten, Distribution and purity of anorthosite across the Orientale basin: New perspectives from Moon Mineralogy Mapper data. *J. Geophys. Res.* **118**, 1 (2013).
73. M. J. Cintala, R. A. F. Grieve, Scaling impact melting and crater dimensions: Implications for the lunar cratering record. *Meteor. Planet. Sci.* **33**, 889 (1998).
74. O. Abramov, S. M. Wong, D. A. Kring, Differential melt scaling for oblique impacts on terrestrial planets. *Icarus* **218**, 906 (2012).
75. P. Lognonné, J. Gagnepain-Beyneix, H. Chenet, A new seismic model for the Moon: Implications for structure, thermal evolution and formation of the Moon. *Earth Planet. Sci. Lett.* **211**, 27 (2003).
76. A. Khan, K. Mosegaard, An inquiry into the lunar interior: A nonlinear inversion of the Apollo lunar seismic data. *J. Geophys. Res.* **107**, 10.1029/2001JE001658 (2002).

77. J. C. Andrews-Hanna *et al.*, Giant dikes and the early expansion of the Moon revealed by GRAIL gravity gradiometry. *Science* **339**, doi: 10.1126/science.1231753 (2013).
78. J. C. Andrews-Hanna *et al.*, Structure and evolution of the lunar Procellarum region as revealed by GRAIL gravity data. *Nature* **514**, doi:10.1038/nature13697 (2014).
79. D. E. Smith *et al.*, Initial observations from the Lunar Orbiter Laser Altimeter (LOLA). *Geophys. Res. Lett.* **37**, doi:10.1029/2010GL043751 (2010).
80. J. W. Head, J. W., C. M. Weitz, L. Wilson (2002), Dark ring in southwestern Orientale basin: Origin as a single pyroclastic eruption, *J. Geophys. Res.* **107**, doi:10.1029/2000JE001438 (2002).
79. The GRAIL mission is supported by NASA's Discovery Program and is performed under contract to the Massachusetts Institute of Technology and the Jet Propulsion Laboratory. Topography was obtained from the Lunar Orbiter Laser Altimeter on the Lunar Reconnaissance Mission, managed by NASA's Goddard Space Flight Center. All data used in this study are archived in the Geosciences Node of the NASA Planetary Data System.

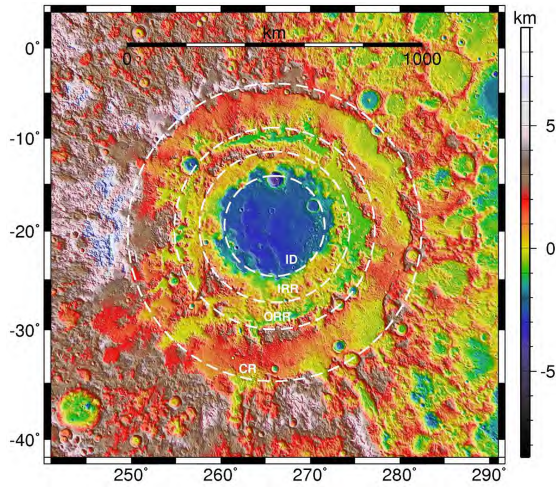
05 May 2016

FIGURE CAPTIONS AND FIGURES

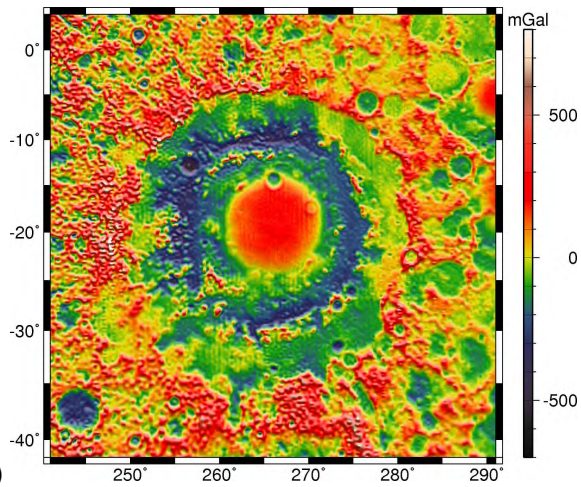
Fig. 1. (A) Topography, (B) free-air anomaly, (C) Bouguer anomaly, (D) crustal thickness, and (E) Bouguer gravity gradient of the Orientale basin and surroundings. Dashed lines in (A) from innermost to outermost correspond to the Inner Depression (ID), Inner Rook ring (IRR), Outer Rook ring (ORR), and Cordillera ring (CR). The solid white line in (D) shows the location of the cross-sectional profile A-A' in Fig. 2a. Blue lines show the locations of the azimuthally averaged cross-sections in Fig. 2b. Topography is updated from Lunar Observer Laser Altimeter (LOLA) (11), map LDEM_64, 0.015625° spatial resolution. To highlight short-wavelength structure, we have subtracted spherical harmonic degrees and orders less than 6 from the Bouguer gravity field. Calculation of crustal thickness and Bouguer gravity gradient are discussed in the SOM.

Fig. 2. (A) Cross-section of the subsurface structure of the Orientale basin along the profile shown in Fig. 1D, from southeast to northwest. Crust is shown as tan, melt sheet as red, and mantle as green. Arrows above the cross-section denote, inward to outward, Orientale's Inner Depression (ID), Inner Rook ring (IRR), Outer Rook ring (ORR), and Cordillera ring (CR). The heavy solid line indicates the base of the crust in the presence of a melt sheet that is 10 km thick, 350 km in diameter, and 2650 kg m^{-3} in density; the thin solid line indicates the base of the crust if the melt sheet density is identical to that of the crust. Vertical exaggeration is 5:1. (B) As in (A), with no vertical exaggeration and 3x higher resolution filter for downward continuation, azimuthally averaged in sectors (azimuth measured clockwise from north, see Fig. 1D) to suppress noise. Red lines give the location of proposed faults dipping inward at 50° dip angle from the nominal surface position of the CRR, ORR, and IRR. Other variations in crust–mantle boundary depth suggest the presence of additional faults.

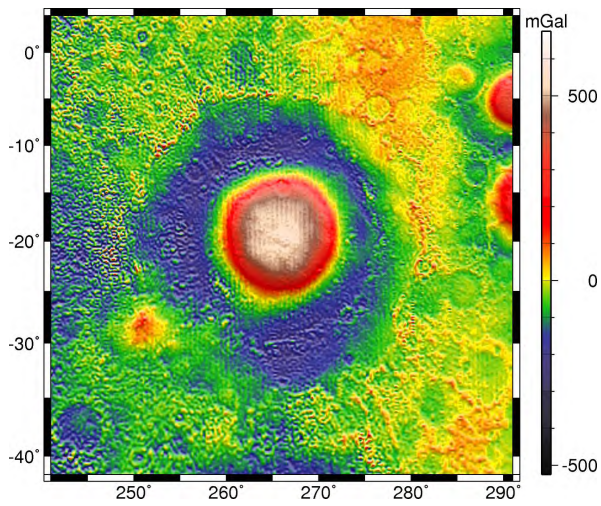
(A)



(B)



(C)



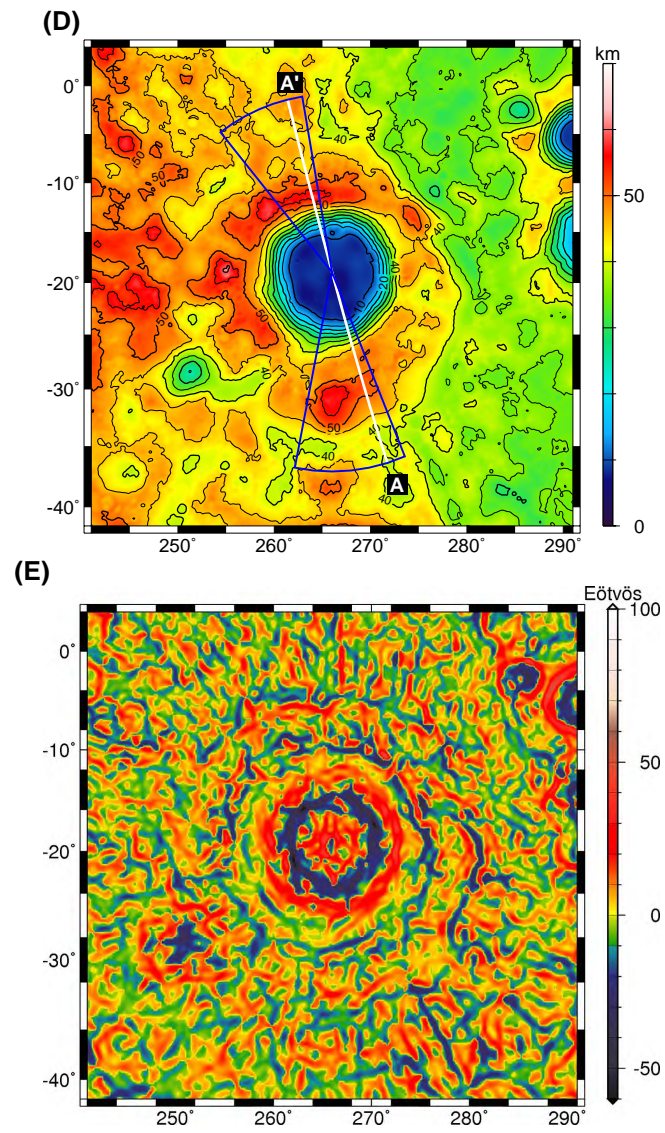


Figure 1
Zuber et al.

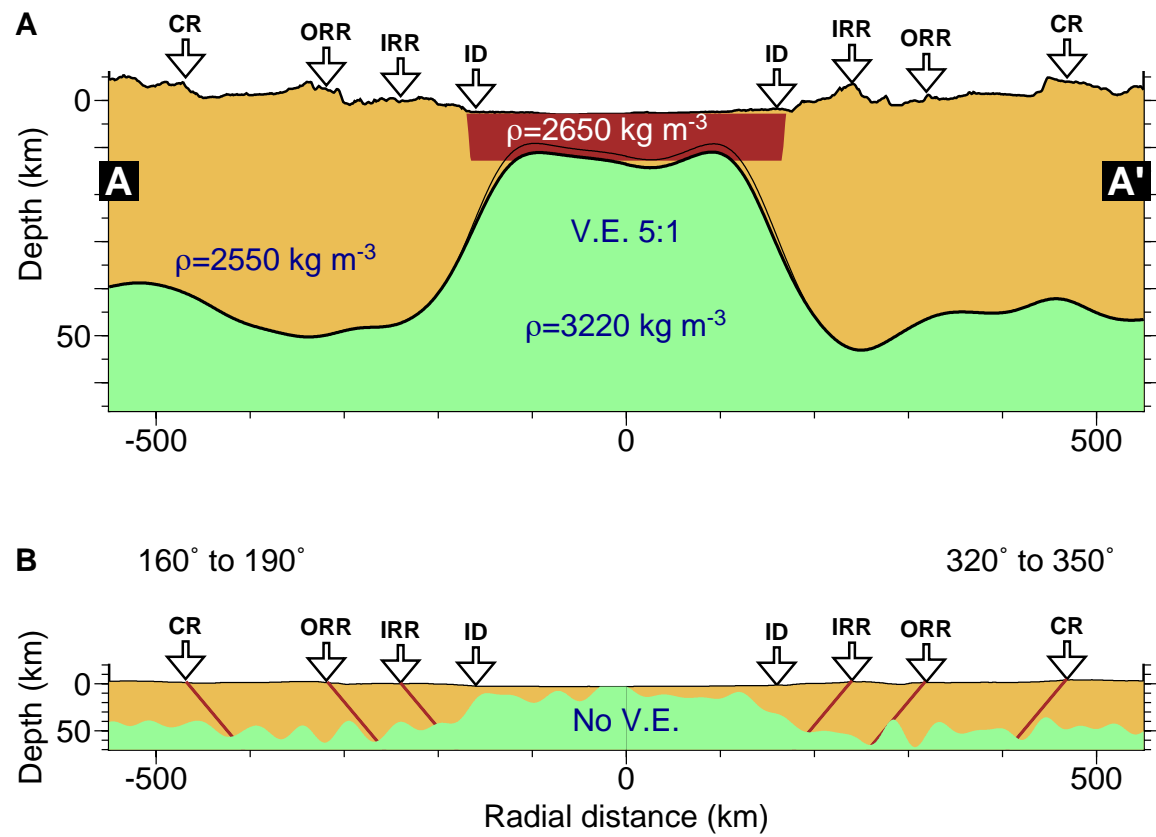


Figure 2
Zuber et al.

Gravity Field of the Orientale Basin from the Gravity Recovery and Interior Laboratory (GRAIL) Mission

Maria T. Zuber^{1*}, David E. Smith¹, Gregory A. Neumann², Sander Goossens³,
 Jeffrey C. Andrews-Hanna^{4,5}, James W. Head⁶,
 Walter S. Kiefer⁷, Sami W. Asmar⁸, Alexander S. Konopliv⁸,
 Frank G. Lemoine², Isamu Matsuyama⁹, H. Jay Melosh¹⁰,
 Patrick J. McGovern⁷, Francis Nimmo¹¹, Roger J. Phillips⁵,
 Sean C. Solomon^{12,13}, G. Jeffrey Taylor¹⁴, Michael M. Watkins^{8,15},
 Mark A. Wieczorek¹⁶, James G. Williams⁸, Johanna C. Jansen⁴,
 Brandon C. Johnson^{1,6}, James T. Keane⁹, Erwan Mazarico²,
 Katarina Miljković^{1,17}, Ryan S. Park⁸, Jason M. Soderblom¹, Dah-Ning Yuan⁸

Supporting Online Material

GRAIL's Mapping Mission

The GRAIL twin spacecraft, Ebb and Flow, orbited in tandem in polar orbit above the Moon and mapped the lunar gravity field at unprecedented resolution and accuracy. After insertion into lunar orbit on December 31, 2011 (Ebb), and January 1, 2012 (Flow), the spacecraft collectively executed a succession of 19 maneuvers to achieve the science orbit and mapping configuration. GRAIL's Primary Mission (PM) (39), which commenced on March 1, 2012, consisted of 89-days of mapping over three 27.3-d global mapping cycles at an orbit inclination of 89.9° and a mean altitude of 55 km. In practice the orbits deviated from circular due to perturbations from the lunar gravity field. When the solar orientation became unfavorable for satellite-to-satellite ranging on May 30, 2012, the spacecraft discontinued mapping and the orbits were raised to a mean altitude of 84 km.

During GRAIL's Extended Mission (XM), which commenced on August 30, 2012, the dual spacecraft orbited above the lunar surface at a mean altitude of 23.5 km (8), less than half the mean mapping altitude in the PM. The low-altitude XM orbit was maintained by executing 2–3 weekly maneuvers (40).

Subsequent to a lunar eclipse on November 28, 2012, the mean altitude of the orbiters was decreased by another factor two to 11.5 km, for additional mapping (Fig. S1). The principal objective of this Endgame mission phase was to perform mapping of the Orientale basin at the highest possible resolution. The low altitude of the spacecraft and variation of topography, coupled with the variability of the lunar gravity field, dictated that the orbital altitude coverage over the basin was non-uniform (Fig. S2), with the lowest altitudes achieved in the eastern part of the basin and in particular over the basin rings, which were mapped from 2-km altitude. GRAIL's science mapping was completed

on December 14, after which a series of engineering experiments was executed prior to deorbit on December 17, 2012.

GRAIL Global Gravity Solutions

The global gravity field of a planetary body is typically represented in spherical harmonics, which are solutions to Laplace's equation for the gravitational potential on a sphere. In practice, the resolution of gravity measured from a spacecraft will depend on both coverage and spacecraft attitude, and so it is common for unmodeled signal to be present even for high-degree and -order gravity field solutions. Published gravity models that incorporate global data from the GRAIL PM are to degree and order 660 (spatial block size = 8.3 km) (41, 42), and published models that incorporate observations from both the PM and XM are to degree and order 900 (spatial block size = 6.0 km) (10, 43). The analysis in this paper uses a degree- and order-1200 (spatial block size = 4.5 km) field (44), produced in the manner of our previously published models. Due to the varying spacecraft altitude that was a combined consequence of the lunar topography and perturbations to spacecraft orbits by the uneven subsurface mass distribution, the full resolution of this global model is achieved only in the areas of lowest-altitude mapping. Orientale contains the lowest-altitude coverage of the GRAIL mission, due to a decision to produce the highest-possible-resolution map of this important structure. The Orientale map from the degree- and order-1200 field was produced at the Jet Propulsion Laboratory (44).

Local Modeling Using Short-arc Analysis

As an alternative approach to achieving the highest-resolution map permitted by the data, we developed a local model of the gravitational signature of Orientale that utilized the residual signal remaining from a gravity model to degree and order 900. We analyzed GRAIL's complete XM and endgame Ka-band range rate (KBRR) tracking data from 240° to 300° E longitude and -55° to 5° latitude. Data were analyzed in arcs of approximately 18-minute duration. The short-arc analysis method (9) utilizes a spherical harmonic representation of the 12-epoch state parameters that quantitatively characterize the baseline between the satellites. First used to determine temporal gravity solutions (45, 46) using data from the Gravity Recovery and Climate Experiment (GRACE) mission (47), the method as applied to the Moon has been demonstrated with GRAIL observations over the lunar south pole (48).

The gravity field may be expressed with the Stokes formulation as a gravitational potential W :

$$W = U + T \quad (1)$$

where U is the normal potential of a reference field and T is the disturbing potential

$$T(P) = \frac{R}{4\pi} \iint_{\sigma} S(P, Q) \Delta g(Q) d\sigma \quad (2)$$

and where the integration is taken over the surface σ , $S(P, Q)$ is the Stokes-Pizetti kernel (49), and the gravity anomalies (Δg) may, with a spherical approximation, be written

$$\Delta g = -\frac{\partial T}{\partial r} - 2\frac{T}{r} \quad (3)$$

where r is the radial distance in spherical coordinates. If T is expressed in spherical harmonics, then the anomalies and spherical harmonics are equivalent and anomalies can

be expressed in spherical harmonics by multiplying by a factor $(l-1)$, where l is the spherical harmonic degree. The partial derivatives of the KBRR data with respect to the anomalies can be obtained from the acceleration on the satellite by differentiating a version of equation (2) in which the integral has been replaced by a summation over the separate anomalies.

Given a GRAIL gravity model to degree and order 900 (10) as an *a priori* model, parameters that included the baseline vector pitch, baseline rate of change of vector magnitude, and baseline rate of change of vector pitch were adjusted using the Goddard Space Flight Center GEODYN II Orbit Determination and Geodetic Parameter Estimation Program (50). After adjusting these baseline parameters and converging the short arcs, GEODYN was again used to calculate partial derivatives of the KBRR data points with respect to the adjusted baseline parameters and selected gravitational field parameters. Local anomaly values (Δg_{adj}) were estimated with respect to the global model ($\Delta g_{GRGM900A}$) at the center coordinates of grid points. For our final model we applied a grid with mixed resolution, to account for the varying altitude above topography. For the area between 240° and 275° E longitude we used a resolution of $0.1667 \times 0.1667 \text{ deg}^2$, whereas for the area between 275° and 300° E longitude, which included the lowest-altitude passes, we used a resolution of $0.1 \times 0.1 \text{ deg}^2$. The maximum spatial resolution is thus 3 to 5 km.

We applied a neighbor-smoothing constraint (51, 52) to the full solution

$$\Delta g_{full} = \Delta g_{adj} + \Delta g_{GRGM900A}, \quad (4)$$

which, in addition to allowing the mapping of gravity anomalies to be extended to the highest resolution, had the benefit of mitigating high-degree striping evident in the spherical harmonic solution. Supercomputers at the NASA Center for Climate Simulation (NCCS) at NASA's Goddard Space Flight Center were used to compute the solutions.

A comparison of residuals from the global spherical harmonic model with those from the local model is shown in Fig. S3 and illustrates the considerable improvement of the latter model. The average root mean square (RMS) residual of the KBRR fits over the Orientale region improves from $0.987 \mu\text{m s}^{-1}$ for the global model to $0.225 \mu\text{m s}^{-1}$ for the local model (77% improvement). The median of the fits improves from $0.629 \mu\text{m s}^{-1}$ to $0.160 \mu\text{m s}^{-1}$ (75% improvement).

Local and Global Map Comparison

The local model and degree-1200 global model are independent representations of the gravitational signature of Orientale produced from the same GRAIL tracking data set. The models are of comparable resolution and, as shown in Fig. S4, they show strikingly similar small-scale structure, which provides high confidence in the short-wavelength character of the map.

Bouguer Anomaly Field and Crustal Structure

In order to isolate subsurface density variations, we subtracted the gravitational attraction of surface topography from a spherical harmonic model to degree and order 1080 to yield a map of Bouguer gravity anomalies. The calculation assumes an upper crustal density of 2550 kg m^{-3} (18) mantle density of 3220 kg m^{-3} . In the Bouguer anomaly plot in Fig. 1C we subtracted spherical harmonic degrees < 6 in order to highlight short-wavelength structure.

Crustal thickness was determined in a manner analogous to an earlier study using GRAIL gravity and LOLA topography by our group (18). In this work we exploit the considerable improvement of the XM data, with more than double the resolution of the data in the earlier study. Downward continuation of the Bouguer anomaly to a crust-mantle interface whose average radius is 1703.15 km yields an average thickness of 34 km and satisfies global constraints. The relief on this density interface produces a gravitational signal that matches the Bouguer anomaly up to a degree and order determined by a constraint on its amplitude needed to regularize the solution in Fig. 2A. This constraint is equivalent to a low-pass filter whose transfer function is 0.5 at degree 80, equivalent to a spatial feature size of ~ 68 km. However, the signal in the anomaly data over Orientale exceeds formal noise estimates at all degrees up to and beyond degree 600, and thus warrants a higher resolution in this region, at the risk of unduly amplifying unmodeled density variations in the near-surface crust. We explored models with 2–3 times higher resolution, whose amplitudes approached the limiting noise level in the data. Spatial averaging over azimuthal sectors, as in Figure 2B, preserves the radial resolution of mantle relief coherent with ring structures, while suppressing signals from the shallower density variations in the crust. The azimuthal sectors shown in Fig. 1D are chosen to avoid large E-W gradients in elevation and crustal thickness.

The range of slopes of the region of uplifted mantle that results from a crustal inversion depends roughly linearly on the density contrast assumed between the crust and mantle. However, the range depends even more on the filter used to stabilize the inversion, with higher slopes generally resulting when higher spherical harmonic degrees are passed by the filter than in the earlier inversion (18). Features that are revealed at higher resolution are suggestive of and consistent with fault displacements in the accompanying hydrocode calculation (14), although faults are virtually indistinguishable from more continuous relief and thus not necessarily required by the data.

Fig. S5 show radial profiles of surface topography and crust-mantle boundary relief that highlights the azimuthal variability of surface and subsurface structure. Within the inner depression, azimuthal variations in thickness are ± 1 km. Outside the Inner Rook ring, azimuthal variations in crustal thickness are ± 5 –10 km, due in large part to azimuthal variability in the topography.

Effect of a High-density Melt Sheet on the Crustal Structure Model

Our crustal structure inversion included a central sheet with higher density than the surrounding crust. This sheet could be representative of crustal impact melt that formed initially with zero porosity, an impact melt sheet that contained both mantle and crustal components, or a more mafic crustal material formed by differentiation of the central impact melt pool.

An end-member model with no melt sheet contribution, a crustal density of 2550 kg m^{-3} , and a mantle density of 3220 kg m^{-3} (18) is consistent with some impact models in which cool crustal material migrates to the basin during basin collapse and covers initially exposed molten mantle material (14, 53). However, because the pre-impact lunar crust is largely to entirely removed by the impact (32), the crust that is measured by GRAIL at the basin center may be dominated by the solidified impact melt sheet.

Impact breccias and impact melt rocks from the Apollo 14, 15, 16, and 17 landing sites provide samples of impact rocks from the Imbrium, Nectaris, and Serenitatis basin-

forming impacts. The measured bulk densities of 18 such rocks range from 2440 to 2830 kg m⁻³ (54). These bulk densities depend primarily on the amount of clastic material with pre-existing porosity in the breccias and the amount of vesicularity within the impact melt. Because of the high level of shock heating in the basin center, we do not expect a large abundance of clasts in the central melt sheet. The Apollo samples have an average melt sheet bulk density of 2720 kg m⁻³ for clast-poor impact melt rocks. Vesicularity should decrease with increasing depth (pressure), so it is possible that a slightly higher average bulk density is appropriate for the melt sheet.

An important consideration is the effect of differences in composition between the Orientale melt sheet and the Apollo impact melt samples. The Apollo samples have a mean FeO concentration of 6.8 weight % (range 3.1 to 9.2 %) and a mean TiO₂ concentration of 0.95 % (range 0.2 to 1.5%), whereas remote sensing observations indicate that the Orientale melt sheet (Maunder Formation) has mean FeO and TiO₂ concentrations of 4.4% and 0.6%, respectively (55). The scaling between composition and grain density of Huang and Wiczorek (56) suggests that the Orientale melt sheet is about 2.4% less dense than the Apollo samples. If the Orientale melt sheet and the Apollo impact melt samples have the same average porosity, this percentage reduction in density can also be applied to the bulk densities, implying a bulk density of 2650 kg m⁻³ for Orientale's melt sheet.

Relative to the typical feldspathic highland crust, the higher melt sheet density reduces the average density difference between crust and mantle and thus requires a thicker crust in the basin center. For a melt sheet density of 2650 kg m⁻³, the minimum crustal thickness in the basin center is 10 km; a denser melt sheet of 2720 kg m⁻³ consistent with Apollo samples yields a minimum crustal thickness of 11 km. These minimum crustal thickness values are 2 and 3 km greater than a model in which the melt sheet has the same density of surrounding feldspathic crust (2550 kg m⁻³). If the crust beneath the basin floor consists of a mixture of feldspathic crust (that either was not excavated or that flowed into the basin center from the surroundings during collapse of the transient cavity) and the impact melt pool, gravity data alone cannot constrain either the relative proportions of these materials or the thickness of the crust beneath the basin floor.

Composition of Crust Excavated by the Orientale Impact

Modeling the structural evolution of the Orientale basin requires knowing the lithologies of the crust beneath the basin. In our modeling we have assumed that anorthositic rock dominates the entire crustal column. However, lunar sample (62) and remote sensing (63) data suggest that in the Procellarum KREEP Terrain [PKT, where KREEP is an acronym for lunar rocks enriched in potassium (K), rare earth elements (REE), and phosphorus (P)], of the lunar nearside, the lower crust is composed of rocks richer in olivine and pyroxene than the upper, plagioclase-rich crust. It is conceivable that this mafic lower crust is present everywhere on the Moon.

We test whether mafic ejecta is present in the Orientale basin and its ejecta using remote sensing data of the region and the expected compositional signature of LKFM. Korotev (64) compiled bulk compositional data for samples of LKFM impact melt breccias from the Apollo 14–17 landing sites. Although compositions vary from site to site, the chief compositional characteristics are well defined: compared with the typical

feldspathic crust, LKFM is significantly enriched in FeO and incompatible trace elements (Th, U, rare earth elements). Mineral abundances also differ: LKFM is enriched in low-Ca pyroxene and depleted in plagioclase compared with the feldspathic highlands. Olivine is variable in abundance and might represent mantle materials incorporated into the LKFM impact melts (64). Bearing in mind that LKFM is a mixture of a KREEP component, anorthosite, and a small component of olivine-rich rock (64), we can use Korotev's (64) compositional compilation and modal analyses of lunar samples (65) as guides to establish a chemical and mineralogical fingerprint of LKFM and use remote sensing data to search the Orientale basin structure for that signature.

Remote sensing data exist for the concentrations of FeO, Th, and major minerals. For FeO concentrations we use maps of Clementine surface reflectance data (binned to 1 km spatial resolution) and an iron-reflectance algorithm (66). For Th we use the Lunar Prospector Gamma-Ray Spectrometer (GRS) dataset (67) gridded at 0.5°, about 15 km spatial resolution. We use mineral data (68), which are derived from radiative-transfer-based mineral maps (69), validated and improved by comparison with Lunar Prospector GRS elemental concentrations gridded to 2° bins. The minerals of interest for detecting mafic impact melt are plagioclase, low-Ca pyroxene, and olivine. The LKFM component contains, as estimated from data compilations (64)-(65), 7–11 wt% FeO, 5–10 ppm Th, 45–50 wt% plagioclase, 25–30 wt% low-Ca pyroxene, and 5–10 wt% olivine. These abundances are similar to the bulk composition of the impact melt sheet hypothesized to be present within the Orientale basin (60). We examined this set of remote chemical and mineralogical data to see if the hypothesized mafic, Th-rich crustal component is present in the Orientale region.

Results are shown in Fig. S6. Fig. S6A shows the topography of Orientale and its surroundings. The Inner Rook ring is outlined for reference and appears on all images in Fig. S6. The mare basalt fill in the middle of Orientale is clearly identifiable by its high FeO concentration (Fig. S6B). The region with lower FeO (~4 wt%) between the maria and the Inner Rook ring composes the Maunder Formation, thought to be impact melt (e.g., (1, 5, 70)). A careful study of the composition of the basin interior (55) indicates that the Maunder Formation has an average FeO concentration of 4.4 ± 2.0 wt%. The Maunder Formation is low (~1.3 ppm) in Th (Fig. S6C), as are all basin deposits, except for the mare basalts. Thus, both FeO and Th concentrations in the exposed Orientale impact melt sheet (the Maunder Formation) are substantially lower than the ranges observed in LKFM rocks or in regions associated with the PKT. We suggest that the low FeO and Th concentrations rule out a significant contribution of mafic lower crustal materials to Orientale surface deposits.

Taking a broad view of the composition of Orientale deposits, the impression is that it is composed of plagioclase-rich rock. All areas (except for the maria) contain at least 70 wt% plagioclase (Fig. S6-D), with many areas containing more than 85%. This result is consistent with the abundance of pure anorthosite in numerous small areas (71, 72). Olivine and orthopyroxene abundances are generally less than 10 wt% and quite variable. Thus, the Orientale basin deposits all appear to be typical lunar feldspathic highlands, with no strong evidence for ejected lower crustal materials. We conclude that the assumption that the crust has the density of porous anorthite (2550 kg m^{-3}) (18), is appropriate for mapping the crustal structure outside of the Inner Rook ring. Within the Inner Depression, where the melt sheet is expected to be thickest, the melt sheet is largely

covered by a thin veneer of mare basalt, and thus remote sensing does not constrain its composition. We therefore used Apollo sample data to estimate the density of the central melt sheet, as described above.

Excavated Volume

In determining the volume of material excavated by the Orientale impact we assumed a mean global crustal thickness of 34 km (18), a crustal density of 2550 kg m^{-3} (which for a 2900 kg m^{-3} grain density yields 12% porosity), and a mantle density of 3220 kg m^{-3} ; these figures collectively satisfy the observations and a 30-km crustal thickness constraint at the sites of the Apollo 12 and 14 seismic stations (75).

In this model the median thickness is 42.7 km in the region surrounding Orientale (Fig. 1D, Fig. 2), and the base of the mantle plug extends to a depth of 43.5 km below the 1738-km-radius topographic datum.

An alternative model with a mean global crustal thickness of 43 km that corresponds to an Apollo seismic constraint of 38 km (76) results in thicker crust at Orientale and a lower mantle density, which would effectively increase the volume of the mantle plug by approximately 10%.

Polar Projections of Orientale

To highlight surface and subsurface deviations from axisymmetry of Orientale, we plot the topography and gravity field in polar coordinates about the basin center. A re-projection of the datasets in Fig. 1 is plotted in Fig. S8. To generate these “unwrapped” maps, we linearly interpolated the topography and gravity datasets on a grid of azimuth (measured clockwise from north) and radial distance with respect to the center of Orientale. The basin center (-19.3°N , 266.0°E) was chosen such that the Bouguer anomaly high at the center of Orientale becomes as close as possible to axisymmetric in this projection. Linear interpolation of the original topography and gravity datasets is necessary in order to smooth the data toward the center of the basin, where latitude and longitude points are relatively widely spaced in an azimuth and radius projection. After this transform, radial features become vertical, parallel lines. Axisymmetric features (e.g., the Cordillera and Inner and Outer Rook rings) become horizontal, parallel lines. Elliptical features and axisymmetric features that are misaligned with the center of Orientale become sinusoids.

As with any two-dimensional Cartesian plot of circular or spherical data, these polar maps can distort relative sizes, shapes, and angles. As we are interested in identifying radial features within Orientale, we used a modified Mercator projection:

$$y = \begin{cases} \ln\left(\tan\left(90^\circ - \frac{\theta}{2}\right)\right) & \text{for } d > 100 \text{ km} \\ (-3.2976 \times 10^{-4})\theta + 4.5479 & \text{for } d < 100 \text{ km} \end{cases}$$

where θ is the angular distance from the center of Orientale (which is related to distance d from the center by $\theta = d / (30.334 \text{ km/degree})$). At radial distances beyond 100 km from the center of Orientale, this projection is conformal (angles are preserved around all locations, and the horizontal and vertical scales around all positions are equal). Thus, the shapes of small features are preserved (e.g., craters are round), although the linear scale changes with distance from the center of Orientale. Like the polar regions of standard Mercator maps, this projection becomes unusable near the basin center. Thus, we use a

linear relationship between y and θ within 100 km, constructed such that $y(\theta)$ is smooth and continuous at 100 km. Although this relation prevents the singularity at $\theta=0^\circ$ found in the Mercator projection, the portion of the map within 100 km of the basin center is not conformal.

Bouguer Gravity Gradients

The gravity gradient quantifies the curvature of the Bouguer gravity field, which can be useful for identifying otherwise hidden density structures in the lunar interior (77, 78). The Bouguer gravity gradient is determined from the Bouguer gravity gradient tensor, which is a nine-component, symmetric tensor with five independent components constructed by taking gradients of the Bouguer gravity field:

$$\bar{\Gamma} \equiv \begin{bmatrix} \frac{\partial g_x}{\partial x} & \frac{\partial g_x}{\partial y} & \frac{\partial g_x}{\partial z} \\ \frac{\partial g_y}{\partial x} & \frac{\partial g_y}{\partial y} & \frac{\partial g_y}{\partial z} \\ \frac{\partial g_z}{\partial x} & \frac{\partial g_z}{\partial y} & \frac{\partial g_z}{\partial z} \end{bmatrix} \equiv \begin{bmatrix} \Gamma_{xx} & \Gamma_{xy} & \Gamma_{xz} \\ \Gamma_{yx} & \Gamma_{yy} & \Gamma_{yz} \\ \Gamma_{zx} & \Gamma_{zy} & \Gamma_{zz} \end{bmatrix},$$

where g_x , g_y , and g_z are the components of the Bouguer gravity field in a local Cartesian reference frame. As we are primarily interested in the horizontal gravity gradients ($\Gamma_{xx}, \Gamma_{xy}, \Gamma_{yy}$), we evaluate the eigenvalues of the horizontal gradient tensor, Γ_{11} and Γ_{22} , which represent the maximum and minimum horizontal curvature of the Bouguer gravity field. We follow Andrews-Hanna et al. (77) and evaluate the maximum amplitude horizontal gravity gradient:

$$\Gamma_{hh} = \begin{cases} \Gamma_{11} & \text{if } \Gamma_{11} > |\Gamma_{22}| \\ \Gamma_{22} & \text{if } \Gamma_{11} < |\Gamma_{22}| \end{cases}.$$

This maximum amplitude eigenvalue (referred to as the ‘‘Bouguer gravity gradient’’ or ‘‘gravity gradient’’ in this paper) effectively quantifies the gravity gradient orthogonal to significant density structures, as long as the structure dominates the local gravity gradients. For this latter criterion to be true, it is necessary that the gravity gradients be evaluated from filtered Bouguer gravity fields to avoid ‘‘striping’’ along the spacecraft trajectory and other sources of noise. The Bouguer gravity was filtered with a low-pass filter applied at degree 600, corresponding to a block size of 9 km. To further smooth the gravity gradients, the field was calculated on a spherical reference surface at a radius of 1740 km, with the upward continuation of the gravity anomalies to this surface having a smoothing effect on shorter wavelengths. At low degree and order, topography in the mantle (such as the mantle uplift beneath Orientale) dominates the curvature in the Bouguer gravity field, and thus the gravity gradient. To highlight shorter wavelengths, and smaller density anomalies, we filtered the Bouguer gravity field with a high-pass filter, removing long-wavelength ($l \lesssim 50$) anomalies. It is important to note that Bouguer gravity gradients can produce spurious features in gravity gradient maps because of the highly non-linear action of evaluating gravity gradients and determining eigenvalues. We have avoided use of the minimum eigenvalue, which is particularly susceptible to this issue.

FIGURE CAPTIONS AND FIGURES

Fig.S1. Apoapsis (green, violet) and periapsis (blue, red) altitudes of GRAIL-A (Ebb) and GRAIL-B (Flow) during the GRAIL mission Endgame phase.

Fig. S2. Minimum altitude above topography of the GRAIL dual spacecraft over the Orientale basin and surroundings.

Fig. S3. **(A)** KBRR residuals with respect to a GRAIL degree-and-order-900 gravity model (10) over the Orientale basin and **(B)** residuals after local modeling for a smoothing factor of 10^{-3} (48).

Fig. S4. Comparison of free-air anomaly fields for the Orientale basin from the GRAIL mission using two independent approaches to achieve high resolution. **(A)** Local model with neighbor smoothing for a scaling factor of 10^{-3} as described by Goossens et al. (48), and **(B)** degree-1200 spherical harmonic solution plotted to degree and order 900.

Fig. S5. Radial profiles of surface topography and mantle relief (in black) across the Orientale basin. Basin center is at far left. Radial averages and standard deviations are plotted in red. The average positions of the basin rings are marked with vertical dashed lines (from left to right): Inner Depression, Inner Rook ring, Outer Rook ring, and Cordillera ring. Vertical exaggeration = 5:1.

Fig. S6. Maps of **(A)** topography, **(B)** FeO concentration, **(C)** Th concentration, **(D)** plagioclase abundance, **(E)** orthopyroxene abundance, and **(F)** olivine abundance for the Orientale basin and nearby areas. The position of the Inner Rook ring is shown in white for reference. Data sources: Topography updated from Lunar Observer Laser Altimeter (LOLA), map LDEM_64, 0.015625° spatial resolution (79); FeO from Clementine 950 nm/750 nm, 1-km data converted to FeO with the algorithm developed by Lucey et al. (66); Th from Lunar Prospector 0.5° data.; mineral maps from Crites and Lucey (68).

Fig. S7. Lunar Reconnaissance Orbiter Wide Angle Camera (LRO/WAC) image [WAC_GLOBAL_E000N1800_032P.img] of the Orientale basin and surroundings showing distribution of highland anorthosite crust (light) and maria (dark; 21). The dark ring in the southern part of the basin centered on the Outer Rook ring is the product of a basaltic pyroclastic eruption from a central vent (80).

Fig. S8. Polar projections of **(A)** topography, **(B)** free-air gravity anomaly, **(C)** Bouguer gravity anomaly, **(D)** crustal thickness, and **(E)** Bouguer gravity gradient with respect to the center of the Orientale basin, encompassing longitudes 240° to 295° E and latitudes -42° to 10°N. This polar projection highlights annular structures, which appear horizontal, and radial structures, which appear as vertical fabric. The center of the basin (-19.3°N, 266.0° E) is stretched along the abscissa at zero radial distance, and the radial distance of 700-km corresponds to the distal extent of the basin. The approximate locations of the Inner Depression (radial distance $r=170.5$ km), Inner Rook ring ($r=240.5$ km), Outer Rook ring ($r=319.5$ km), and Cordillera ($r=468.5$ km) are indicated by dashed lines.

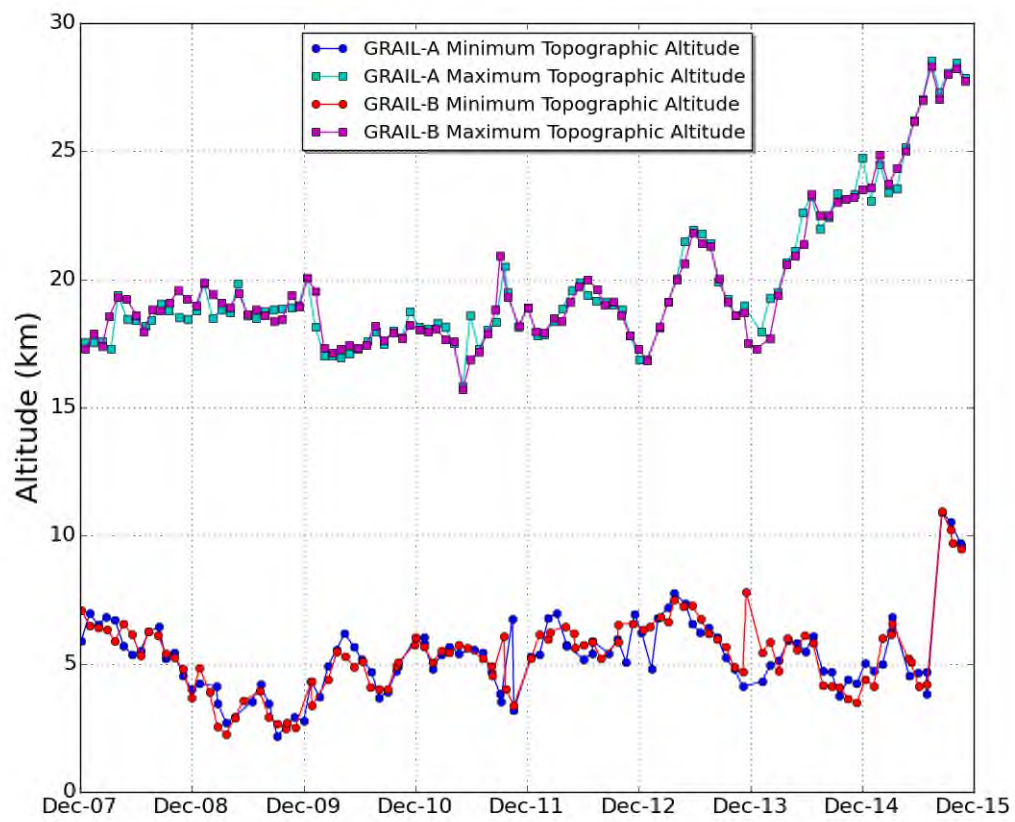


Figure S1
Zuber et al.

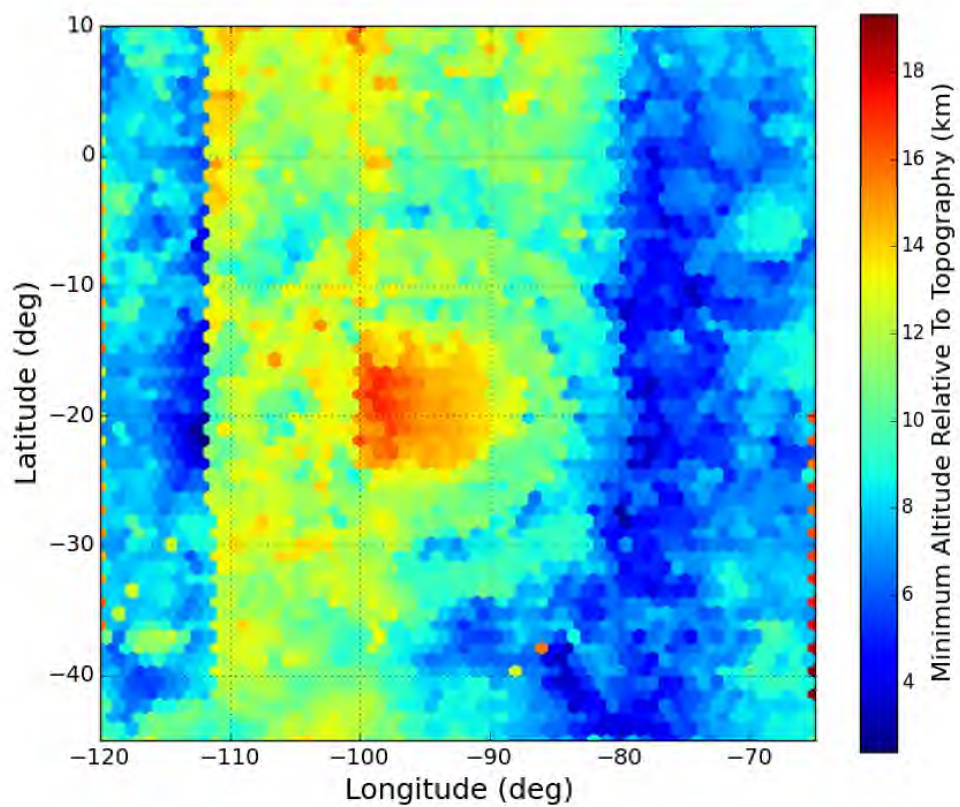


Figure S2
Zuber et al.

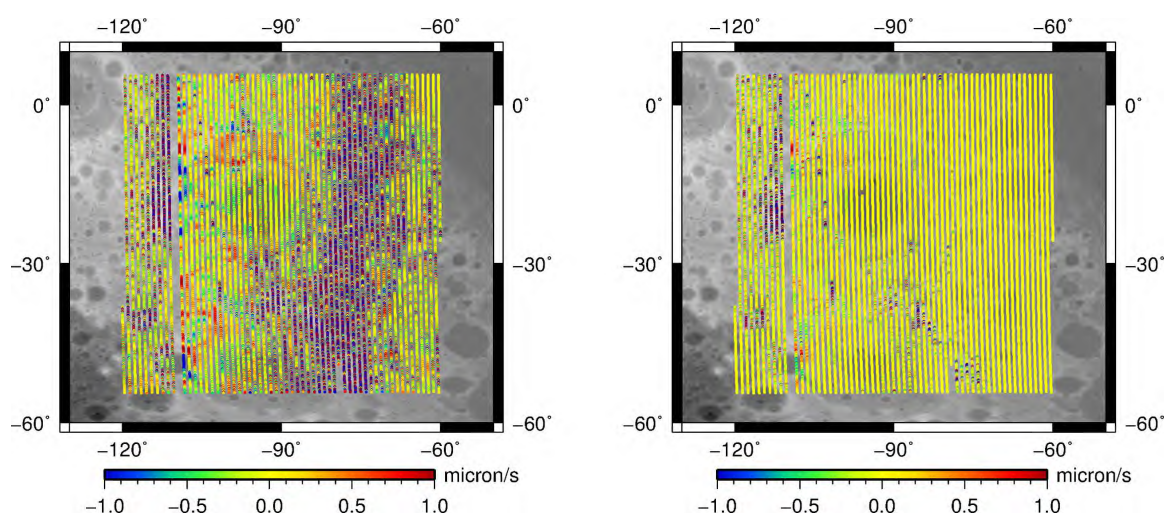


Figure S3
Zuber et al.

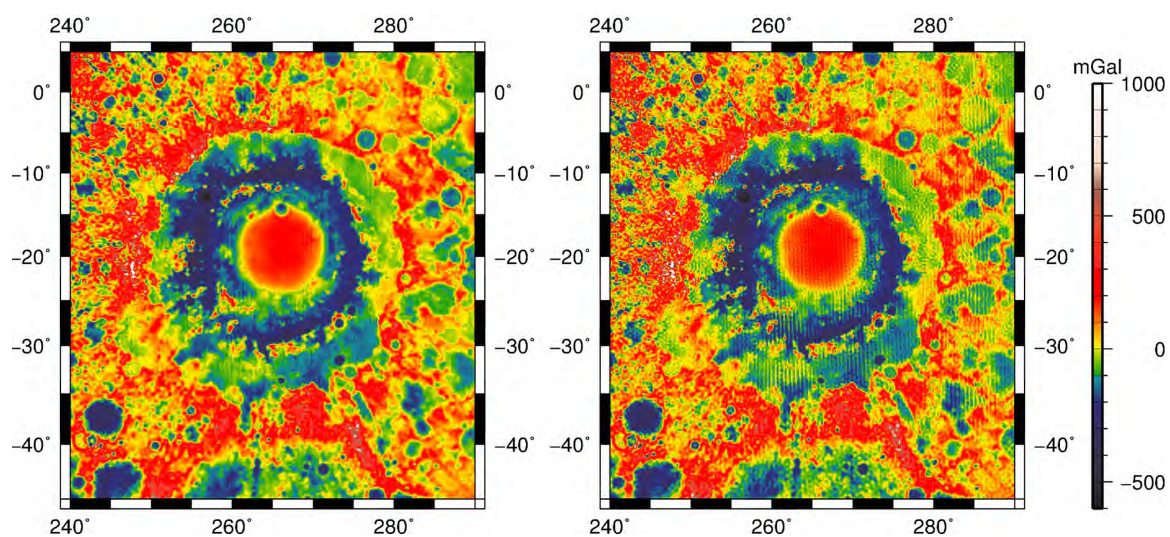


Figure S4
Zuber et al.

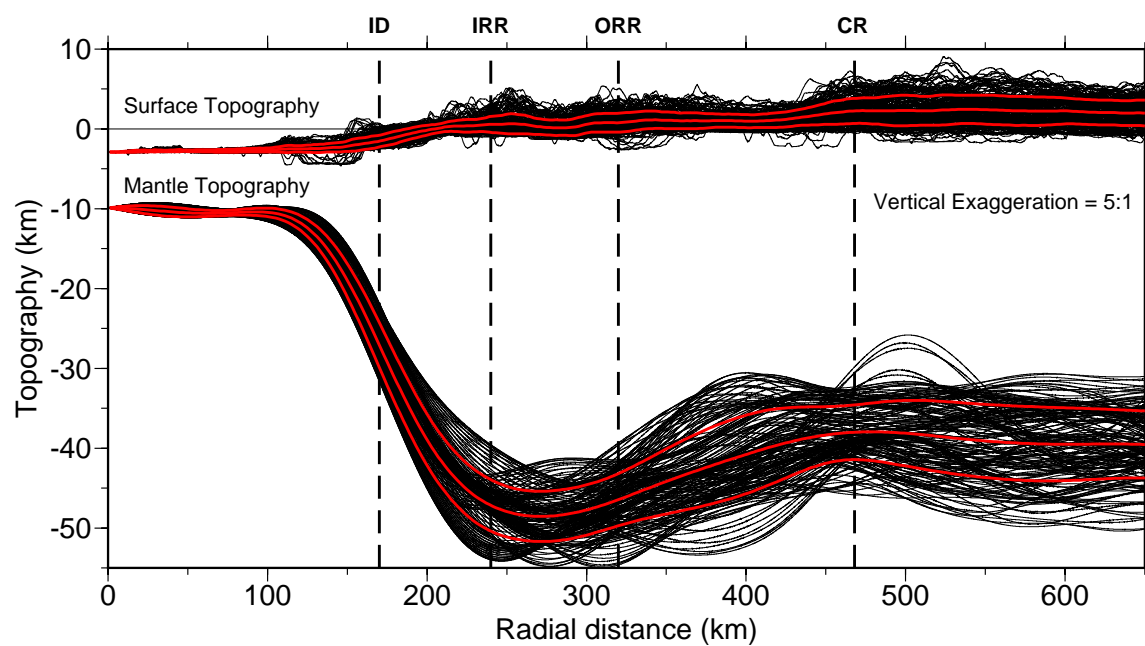


Figure S5
Zuber et al.

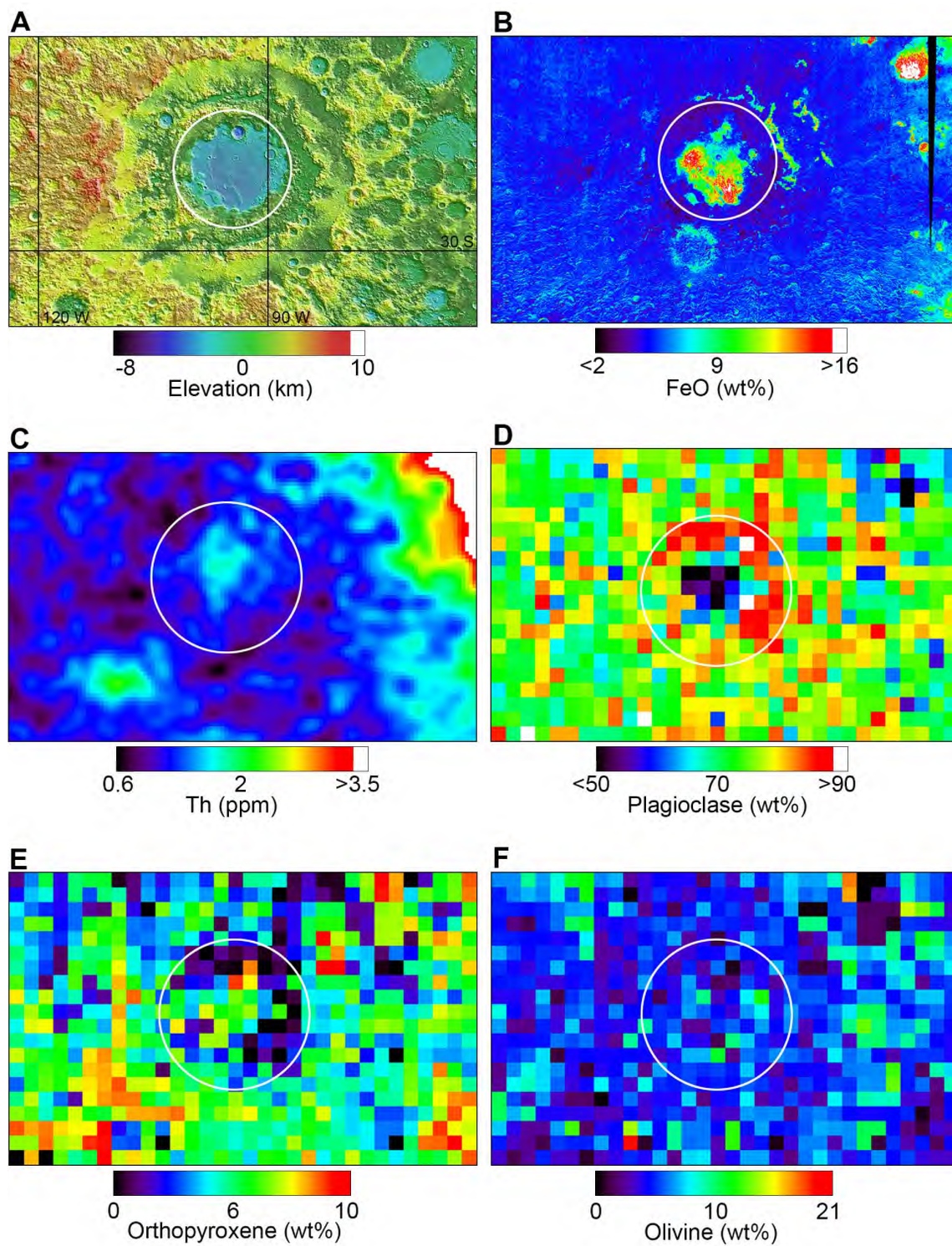


Figure S6
Zuber et al.

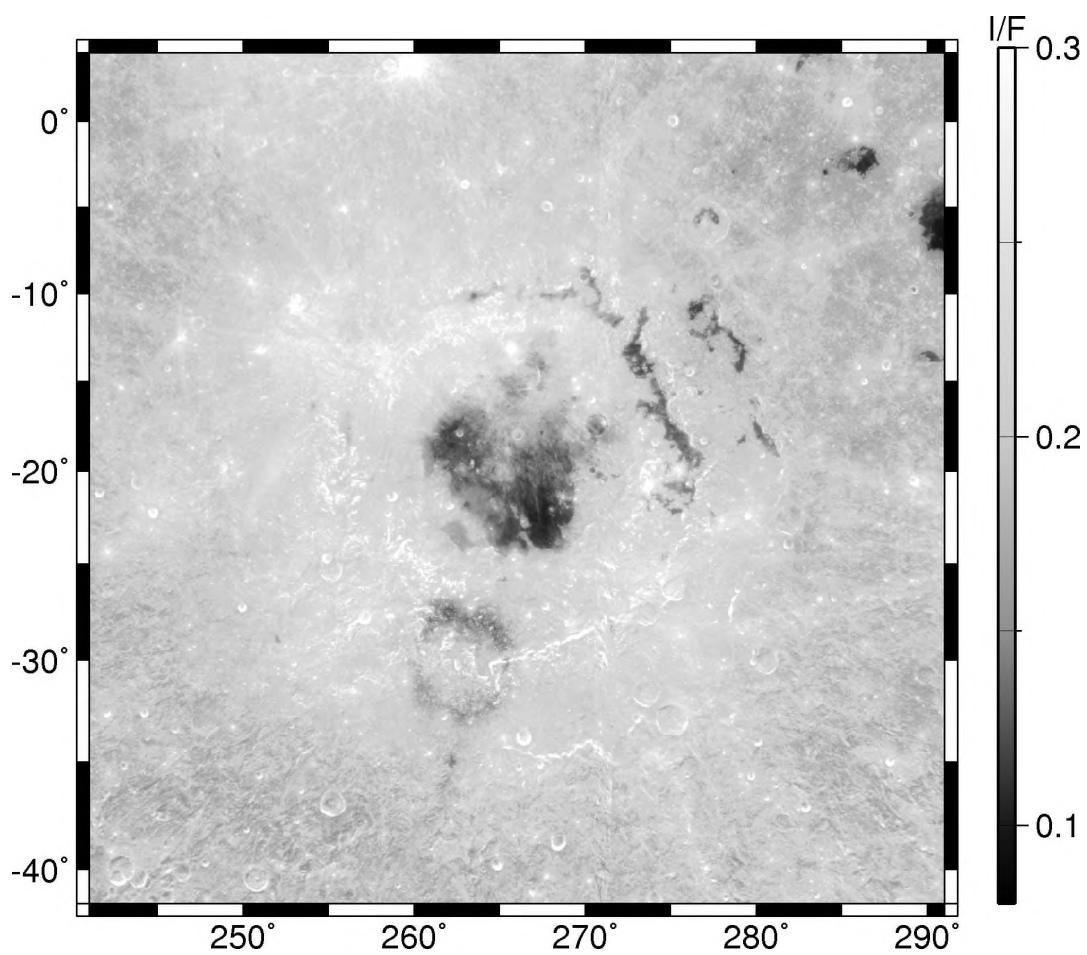


Figure S7
Zuber et al.

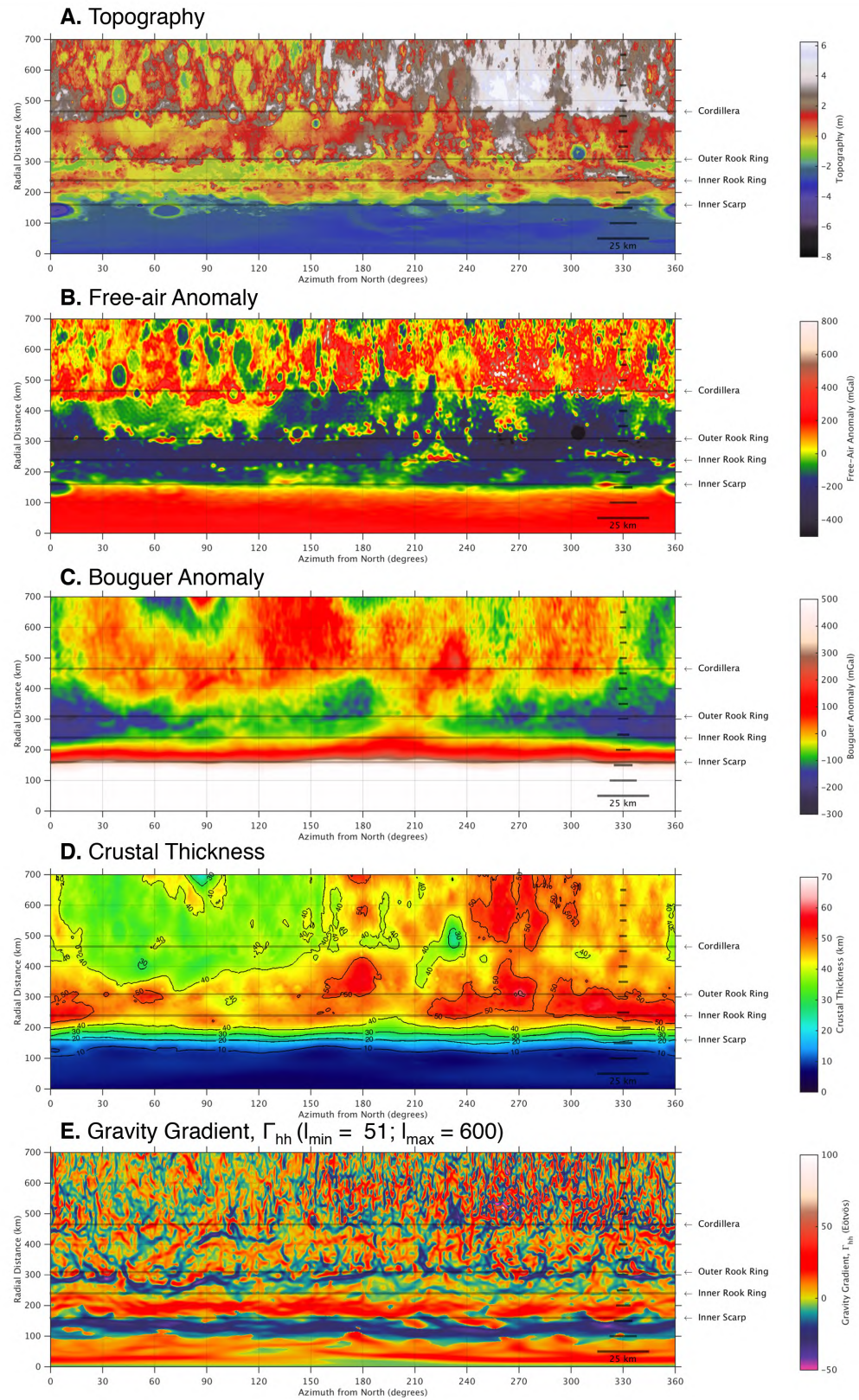


Figure S8
Zuber et al.